Inverse-Based Local Loop Shaping and IIR-Filter Design For Precision Motion Control

Xu Chen * **Atsushi Oshima** ** **and Masayoshi Tomizuka** *

* *Department of Mechanical Engineering, University of California, Berkeley, CA, 94720, USA (e-mails: {maxchen,tomizuka}@me.berkeley.edu).*
** *Mechatronics Development Center, NSK Ltd, Fujisawa, Kanagawa 251-8501, Japan (email:atsuoshi508@gmail.com)*

Abstract: In motion-control problems such as vibration rejection, periodical reference tracking, and harmonic disturbance cancellation, the disturbances/references share a common characteristic of exhibiting concentrated energies at multiple bands of frequencies. In this paper, we discuss a feedback loop-shaping approach to address such a class of control problem. An integration of (inverse) system models is proposed to bring enhanced high-gain control at the required local frequency regions. We show that such servo enhancement can be effectively achieved if good model information is available at the disturbance frequencies, and that a rich class of design tools can be integrated for the controller formulation. The proposed algorithm is verified in simulation and experiments on vibration rejection in hard disk drives and an electrical power steering system in automotive vehicles.

Keywords: digital control, vibration rejection, digital-filter design, loop shaping, hard disk drives, electrical power steering

1. INTRODUCTION

Driven by the ever increasing demand for higher accuracy, faster speed, and more robust performance, customized control design is becoming more and more essential in precision-motion-control systems. For example, in the application to all-in-one personal computers and smart TVs, modern hard disk drives (HDDs) are placed close to high-power audio speakers that generate a significant amount of vibrations. Due to the nature of the disturbances (Deller et al., 1999), these vibrations occur in several concentrated bands of frequencies, near or even above the bandwidth of the servo system. Fig. 1 demonstrates the impact of actual audio vibrations on an HDD benchmark problem (IEEJ, Technical Commitee for Novel Nanoscale Servo Control, 2007). Despite the fact that a set of baseline controllers have been designed to meet standard industrial requirements, [1] in the presence of strong vibrations, we observe that common feedback design has difficulty attenuating the local spectral peaks at around 880 Hz and 1600 Hz. The servo challenge is additionally amplified by the increasing demand on servo accuracy, as the HDD disk density continues growing to meet the requirements in modern and future data storage applications.

A related type of disturbance, with its spectral peaks much sharper than those in Fig. 1, is the narrow-band disturbance consisting of single-frequency vibrations. Such disturbance is common in motion control that involves periodic movements. Examples include but are not limited

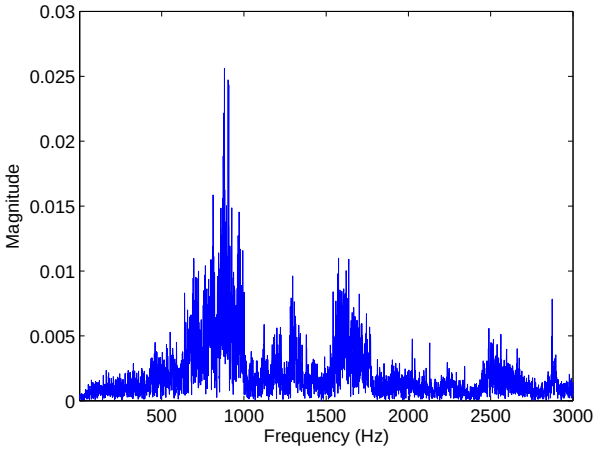

Fig. 1. A typical HDD error spectrum under vibrations

to: (i) engine noise in turboprop aircraft and automobiles (Shoureshi and Knurek, 1996) (ii) repeatable runout, disk flutter, and fan noise in HDDs (Ehrlich and Curran, 1999; Guo and Chen, 2001) (iii) vibration in suspension systems (Landau et al., 2009) and (iv) repetitive trajectory tracking (Tomizuka, 2008). Customized servo design is essential for attenuating these disturbances.

From the feedback-control perspective, both reference tracking and disturbance attenuation are about shaping the dynamic behavior of the servo loop. Based on the spectral properties, we will regard narrow-band disturbances, and vibrations that generate residual errors similar to that

[1] A set of notch filters and an PID controller have been applied to attenuate the resonances and achieve a 1.19kHz bandwidth here.

in Fig. 1, as to belong to the same class of signals. We denote such disturbances as *band-limited disturbances*, and the corresponding closed-loop control design as *local loop shaping*.

The application of inverse system models is proposed to address the aforementioned problem. Inverse-based control has long been used in motion control (for example, in feedforward designs), but not extensively explored in feedback vibration rejection, especially for attenuating audio vibrations. Different from narrow-band loop shaping that can be achieved via e.g., peak filters (Zheng et al., 2006), repetitive control (Chew and Tomizuka, 1989; Cuiyan et al., 2004), Youla parameterization (Landau et al., 2009), and narrow-band disturbance observers (Chen and Tomizuka, 2012), general band-limited vibrations are much more challenging to reject, since enhanced local loop shape is usually accompanied by deteriorated servo performance at other frequencies. This is the "waterbed effect" from Bode's Integral Theorem. To balance between the desired vibration rejection and the theoretical boundaries, we investigate methods to place a group of structured poles and zeros for local loop shaping, and provide the design of infinite-impulse-response (IIR) digital filters to reduce the disturbance amplification.

The remainder of the paper is organized as follows. Section 2 discusses the controller structure and the loop-shaping idea. Section 3 provides the customized filter design techniques. Section 4 shows the simulation and experimental results on vibration rejection. Section 5 concludes the paper.

2. CONTROLLER STRUCTURE

Consider a general discrete-time feedback system with the plant and the stabilizing negative-feedback controller given by $P(z^{-1})$ and $C(z^{-1})$ respectively. In motion control, $C(z^{-1})$ is designed such that $y(k)$, the output of the plant, tracks the reference $r(k)$ while rejecting the disturbance $d(k)$. Corresponding, at frequencies below the bandwidth of the closed loop, the complementary sensitivity function $T_o(z^{-1}) = G_{r\to y}(z^{-1}) = P(z^{-1})C(z^{-1})/[1 + P(z^{-1})C(z^{-1})]$ approximates unity and the sensitivity function (a.k.a. the output disturbance-rejection function) $S_o(z^{-1}) = 1-T_o(z^{-1}) = 1/[1+P(z^{-1})C(z^{-1})]$ should have small magnitude at locations where $d(k)$ presents large spectral peaks.

Consider adding three elements $z^{-m}\hat{P}^{-1}(z^{-1})$, z^{-m}, and $Q(z^{-1})$ around $C(z^{-1})$ as shown in Fig. 2. Computing the new sensitivity and complementary sensitivity functions gives (due to space limit, we drop the index (z^{-1}) here)

$$T = \bar{G}_{r\to y} = \frac{PC + z^{-m}Q\hat{P}^{-1}P}{1 + PC + z^{-m}Q(\hat{P}^{-1}P - 1)} \tag{1}$$

$$S = 1 - T = \frac{1 - z^{-m}Q}{1 + PC + z^{-m}Q(\hat{P}^{-1}P - 1)}. \tag{2}$$

Here $\hat{P}^{-1}(z^{-1})$ is defined as the inverse model of $P(z^{-1})$. We add the delay element z^{-m} so that $z^{-m}\hat{P}^{-1}(z^{-1})$ is realizable if the relative degree of $P(z^{-1})$ is larger than zero in Fig. 2. $\hat{P}^{-1}(z^{-1})$ is assumed to be stable. This is practically not difficult to satisfy for motion-control systems (see, e.g., Ohnishi et al. (1996); Tomizuka (1987)). For the case of unstable $P^{-1}(z^{-1})$, a related discussion of optimal inverse design is provided in Chen et al. (2013).

To see the role of $Q(z^{-1})$, note first that when $\hat{P}^{-1}P = 1$, (1) and (2) reduce to

$$T(z^{-1}) = \frac{P(z^{-1})C(z^{-1}) + z^{-m}Q(z^{-1})}{1 + P(z^{-1})C(z^{-1})}. \tag{3}$$

$$S(z^{-1}) = \frac{1 - z^{-m}Q(z^{-1})}{1 + P(z^{-1})C(z^{-1})} \tag{4}$$

If in addition $z^{-m}Q(z^{-1}) = 1$, then we have $S(z^{-1}) = 0$ and $T(z^{-1}) = 1$ in the above equations, i.e., perfect disturbance rejection and reference tracking. Furthermore, the right hand side of (4) equals $S_o(z^{-1})(1-z^{-m}Q(z^{-1}))$, where $S_o(z^{-1})$ is the baseline sensitivity function computed at the end of the first paragraph in this section. $S(z^{-1})$ is hence decomposed to have the additional freedom to shape the loop via $1 - z^{-m}Q(z^{-1})$, while the original sensitivity function $S_o(z^{-1})$ remains intact.

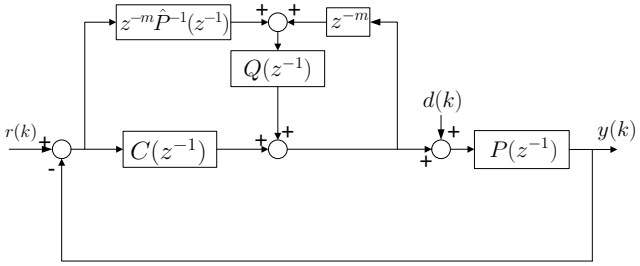

Fig. 2. Block diagram of proposed loop shaping

The above is an ideal-case analysis due to the perfect-model assumption. The condition $z^{-m}Q(z^{-1}) = 1$ is also not practical as it requires an anti-causal $Q(z^{-1}) = z^m$. However, replacing every z^{-1} with $e^{-j\omega}$ and re-evaluating the equations, we see that (4) and (3) still hold in the frequency domain provided that $\hat{P}^{-1}(e^{-j\omega})P(e^{-j\omega}) = 1$. At this specific ω value, we still have $S(e^{-j\omega}) = 0$ and $T(e^{-j\omega}) = 1$ if $e^{-mj\omega}Q(e^{-j\omega}) = 1$. Therefore, enhanced local loop shaping remains feasible at the frequency regions where good model information is available. At the frequencies where there are large model mismatches, efficient servo control is intrinsically difficult from robust-control theory. We will thus make $e^{-mj\omega}Q(e^{-j\omega}) \approx 0$, to keep the influence of the uncertainty elements $e^{-jm\omega}Q(e^{-j\omega})\hat{P}^{-1}(e^{-j\omega})P(e^{-j\omega})$ and $z^{-m}Q(e^{-j\omega})[\hat{P}^{-1}(e^{-j\omega})P(e^{-j\omega}) - 1]$ small in (2) and (1). More formally, if the plant is perturbed to $\tilde{P}(e^{-j\omega}) = P(e^{-j\omega})\left(1 + \Delta(e^{-j\omega})\right)$,[2] standard robust-stability analysis (see, e.g., Chap. 7.5 of Skogestad and Postlethwaite (2005)) gives that the closed-loop system is stable if and only if the following hold:

- nominal stability–the closed loop is stable when $\Delta(e^{-j\omega}) = 0\ \forall\omega$, i.e., the nominal Nyquist plot has the correct number of encirclements around (-1,0) in the complex plane, and does not touch (-1,0).
- robust stability–$\forall\omega$, $\left|\Delta(e^{-j\omega})T(e^{-j\omega})\right| < 1$, where T is given by (1). This additionally guarantees that

[2] Δ is assumed to be stable and has finite magnitude response.

the perturbed Nyquist plot does not touch the (-1,0) point.

From (4) and (3) we see that nominal stability is satisfied as long as $Q(z^{-1})$ is stable. If $Q(e^{-j\omega}) = 0$, the add-on loop shaping is essentially cut off in Fig. 2, and (1) reduces to $T(e^{-j\omega}) \approx T_o(e^{-j\omega})$. We thus have $\left|\Delta(e^{-j\omega})T(e^{-j\omega})\right| \approx \left|\Delta(e^{-j\omega})T_o(e^{-j\omega})\right| < 1$, which is the robust stability condition for the baseline feedback loop, and is satisfied by our assumption that $C(z^{-1})$ is a stabilizing controller.

To summarize, in regions where good model information is available, $e^{-jm\omega}Q(e^{-j\omega}) \approx 1$ in (4) gives small gain in $S(e^{-j\omega})$ and we have enhanced servo performance at this local frequency region; at frequencies where vibrations do not occur or there are large model mismatches, letting $e^{-jm\omega}Q(e^{-j\omega}) \approx 0$ maintains the original loop shape and system stability. This concept will be the central of our discussions in the following sections.

Finally we remark that when $P(z^{-1})$ is minimum-phase then the proposed controller structure forms a special Youla parametrization (see e.g., Zhou and Doyle (1998)), [3] which indicates that any controller that stabilizes the feedback system can be formed by picking some stable $Q(z^{-1})$ in Fig. 2. The design of this Q filter in Youla parametrization however does not have a common rule. With the plant inversion already achieved by $\hat{P}^{-1}(z^{-1})$, the next section discusses how we can incorporate structured designs in $Q(z^{-1})$ for band-limited local loop shaping.

3. BAND-LIMITED LOCAL LOOP SHAPING

3.1 General Concept

Recall from Fig. 1, that band-limited disturbances show peaks in the error spectrum. To introduce small gains at these local frequencies in the sensitivity function (4), we consider the following design on $Q(z^{-1})$:

$$1 - z^{-m}Q(z^{-1}) = \frac{A(z^{-1})}{A(\alpha z^{-1})}K(z^{-1}) \tag{5}$$

$$Q(z^{-1}) = \frac{B_Q(z^{-1})}{A(\alpha z^{-1})} \tag{6}$$

where $0 < \alpha < 1$ and

$$A(\gamma z^{-1}) \triangleq 1 - 2\gamma\cos\omega_0 z^{-1} + \gamma^2 z^{-2},\ \gamma = 1, \alpha \tag{7}$$

$$= \left(1 - \gamma e^{j\omega_0} z^{-1}\right)\left(1 - \gamma e^{-j\omega_0} z^{-1}\right). \tag{8}$$

From the factorization (8), $A(z^{-1})/A(\alpha z^{-1})$ in (5) is a special notch filter, with its zeros and poles respectively given by $e^{\pm j\omega_0}$ and $\alpha e^{\pm j\omega_0}$. ω_0 is in the unit of radians here, and equals $2\pi\Omega_0 T_s$ (Ω_0 is in Hz, T_s is the sampling time in sec). The zeros $e^{\pm j\omega_0}$ provide small gains in $A(z^{-1})/A(\alpha z^{-1})$ around the center frequency ω_0 (can check that $A(e^{-j\omega_0}) = 0$ from (8)). The poles $\alpha e^{\pm j\omega_0}$ balance the magnitude response such that $A(e^{-j\omega})/A(\alpha e^{-j\omega}) \approx 1$ when ω is far away from ω_0. The structured poles and zeros in (5) will be absorbed to the sensitivity function due to the construction of (4), and provides the desired local modification to the loop shape. Approximately, the -3dB bandwidth for this notch filter is given by $(1 - \alpha^2)/[(\alpha^2 + 1)(\pi T_s)]$. The notch shape of $|A(e^{-j\omega})/A(\alpha e^{-j\omega})|$ becomes sharper and sharper as α gets closer to 1.

We will demonstrate the placing of one notch shape in the sensitivity function. The design of placing multiple notches is analogous after replacing (7) with $A(\gamma z^{-1}) = \prod_{i=1}^{n}(1 - 2\gamma\cos\omega_i z^{-1} + \gamma^2 z^{-2})$.

In (5), the plant delay m is usually non-zero for practical control systems. $K(z^{-1})$ functions in this case to satisfy the causality of $Q(z^{-1})$: without $K(z^{-1})$, equations (5-7) give

$$Q(z^{-1}) = \frac{(\alpha^2 - 1)z^{-2+m} - (\alpha - 1)\,2\cos\omega_0 z^{-1+m}}{1 - 2\alpha\cos\omega_0 z^{-1} + \alpha^2 z^{-2}} \tag{9}$$

which contains the unrealizable term z^{-1+m} if $m > 1$.

Assigning $K(z^{-1}) = k_0 + k_1 z^{-1} + \cdots + k_{n_K} z^{-n_K}$ (an FIR filter) reduces (5) to

$$A(z^{-1})K(z^{-1}) + z^{-m}B_Q(z^{-1}) = A(\alpha z^{-1}) \tag{10}$$

where $A(z^{-1})$, z^{-m}, and $A(\alpha z^{-1})$ are known from the previous design. Matching the coefficients of z^{-1}, we can solve for $B_Q(z^{-1})$ and $K(z^{-1})$. [4] The minimum-order solution satisfies $\deg(B_Q(z^{-1})) = \deg(K(z^{-1})) + \deg(A(z^{-1})) - m$ and $\deg(A(\alpha z^{-1})) \le \deg(B_Q(z^{-1})) + m$.

The dashed line in Fig. 3 presents an example of the solved $Q(z^{-1})$ and $1 - z^{-m}Q(z^{-1})$, with $\alpha = 0.993$, $T_s = 1/26400$ sec, $\Omega_0 = 3000$ Hz, and $m = 2$. We observe that $1 - z^{-m}Q(z^{-1})$ is approximately unity except at the desired attenuation frequency $\Omega_0 = 3000$ Hz, where we have $1 - e^{-mj\omega_0}Q(e^{-j\omega_0}) = K(e^{-j\omega_0})A(e^{-j\omega_0})/A(\alpha e^{-j\omega_0}) = 0$ due to $A(e^{-j\omega_0}) = 0$ in (8). Thus, from (2), $S(e^{-j\omega_0}) = 0$ and disturbances at 3000 Hz gets perfectly attenuated. Meanwhile, the magnitude of $Q(z^{-1})$ reduces from 1 at 3000 Hz quickly down to -35dB (0.0178 in absolute value) in the low-frequency region, and -50dB (0.0032) in the high-frequency region. As discussed in the last section, these small gains reduce the influence of the model uncertainties, so that (4) and (3) are valid approximations of (2) and (1).

With the same center-frequency configuration, the solid line in Fig. 3 shows the solved $Q(z^{-1})$ and $1 - z^{-m}Q(z^{-1})$ for $\alpha = 0.945$. For this $Q(z^{-1})$, the width of the pass band at -3dB is approximately 475 Hz. We can see that the desired loop shaping is also effectively achieved, and that such a $Q(z^{-1})$ suits for rejecting disturbances with wide spectral peaks such as the one described in Fig. 1.

Using the designs in Fig. 3, if we consider a standard feedback design of $1/(1 + P(z^{-1})C(z^{-1}))$ and use (4), we obtain the magnitude responses of $S(z^{-1})$ in Fig. 4. The dotted line is the magnitude response of $S_o(z^{-1}) = 1/(1 + P(z^{-1})C(z^{-1}))$. In this example, we used a loop shape that is common for motion control. The solid and the dashed lines are the magnitude responses of $S(z^{-1})$ after we introduce the proposed designs in Fig. 3. We observe that the shape of $1 - z^{-m}Q(z^{-1})$ is directly reflected to $S(z^{-1})$ due to the relationship $S(z^{-1}) \approx S_o(z^{-1})(1 - z^{-m}Q(z^{-1}))$.

[3] The proof is omitted here due to space limit.

[4] (10) is a Diophantine equation. Some existing solvers are provided in Landau and Zito (2006).

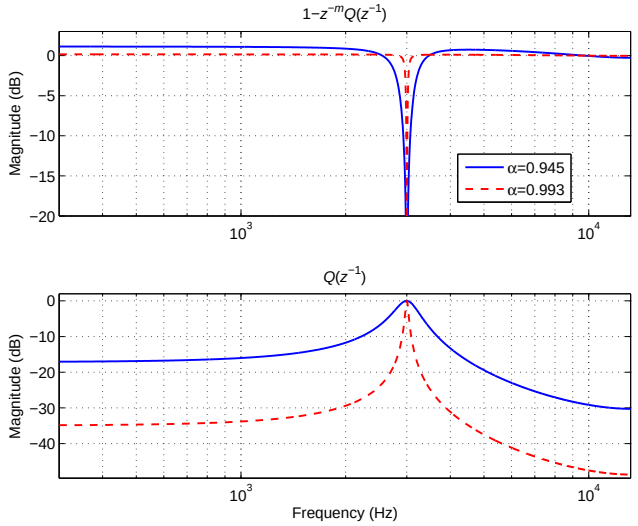

Fig. 3. Magnitude responses of two example $Q(z^{-1})$'s and the corresponding $1 - z^{-m}Q(z^{-1})$'s

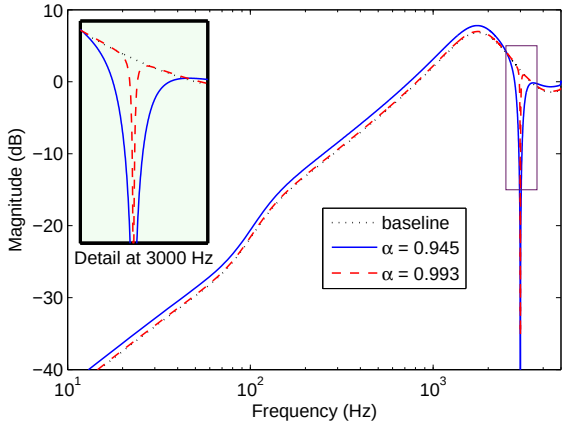

Fig. 4. Magnitude responses of the sensitivity functions with the designs in Fig. 3

3.2 Additional Customization

It is not practical to have an ideal bandpass filter that equals either unity or zero at each frequency. In Fig. 3, as the magnitude response of $Q(z^{-1})$ gets sharper and sharper, we more and more approximate an ideal filter that passes only the frequency component at 3000 Hz. In order to achieve the solid line, i.e., a larger-bandwidth $Q(z^{-1})$, and hence a wider range of attenuation frequencies in Fig. 4, the computation of (10) has traded off the small magnitudes of $Q(z^{-1})$ at frequencies far away from 3000 Hz. As a result,

- in the top plot of Fig. 3, the solid-line $|1 - e^{-jm\omega}Q(e^{-j\omega})|$ becomes larger than unity at low and high frequencies;
- the robustness of the algorithm against plant uncertainty is decreased as the term $z^{-m}Q(\hat{P}^{-1}P-1)$ may become not negligible in (2).

These concerns will not occur in narrow-band loop shaping, where the bandwidth of $Q(z^{-1})$ is very small, but should be examined with care in the case of rejecting general band-limited disturbances. We discuss next methods to reduce the above design trade offs.

3.2.1 The effect of fixed zeros in $Q(z^{-1})$

In Section 3.1, we chose the IIR $Q(z^{-1})$ with a customized denominator $A(\alpha z^{-1})$ but have not placed specific structural designs for $B_Q(z^{-1})$. Actually $B_Q(z^{-1})$ is the unknown to be solved in (10) and its nontrivial frequency response is solely determined by the algebraic equation. Using the concept in pole placement, we can add a fixed part $B_0(z^{-1})$ such that

$$B_Q(z^{-1}) = B_0(z^{-1})B_Q^{'}(z^{-1}). \tag{11}$$

Designing $B_0(z^{-1}) = 1 + z^{-1}$ for example, will yield $Q(e^{-j\omega})\big|_{\omega=\pi} = B_Q(-1)/A(-\alpha) = 0$, i.e., zero magnitude at Nyquist frequency. More generally, introducing fixed zero near $z = -1$ and/or $z = 1$ in the z plane will provide enhanced small gains for $Q(z^{-1})$ in the high- and/or low-frequency region. Extending this idea, we can essentially place magnitude constraints at arbitrary desired frequencies, by letting $B_0(z^{-1}) = 1-2\beta\cos\omega_p z^{-1}+\beta^2 z^{-2}$ in (11), which places the fixed zeros $\beta e^{\pm j\omega_p}$ to penalize $\left|Q(e^{-j\omega})\right|$ near $\omega = \omega_p$.

Table 1 summarizes the effects of different configurations for the fixed term $B_0(z^{-1})$. For band-limited loop shaping, it is natural to place magnitude constraints at both low and high frequencies. In this case, the modules in Table 1 can be combined to provide, e.g., $B_0(z^{-1}) = \left(1+\rho z^{-1}\right)^{n_1}\left(1-z^{-1}\right)^{n_2}$, where $\rho \in [0.5, 1]$; and n_1, n_2 are non-negative integers.

Table 1. Effects of placing fixed zeros to $Q(z^{-1})$

$B_0(z^{-1})$	zeros	small $\lvert Q(e^{-j\omega})\rvert$
$1 + z^{-1}$	-1	around Nyquist freq.
$1 + \rho z^{-1},\ \rho \in [0.5, 1]$	$-\rho$	at high freq.
$1 - \rho z^{-1},\ \rho \in [0.5, 1]$	ρ	at low freq.
$1 - 2\beta\cos\omega_p z^{-1} + \beta^2 z^{-2}$ $\beta \in (0, 1]$	$\beta e^{\pm j\omega_p}$	around ω_p
$1 - z^{-1}$	1	at low freq.

3.2.2 Cascading a bandpass IIR filter to $Q(z^{-1})$

By (11) we essentially have cascaded the FIR filter $B_0(z^{-1})$ to $Q(z^{-1})$. $B_0(z^{-1})$ has been designed to control the magnitude response of $Q(z^{-1})$ at some specific frequency regions. It is well known that IIR design has additional flexibility compared to FIR filters. From the frequency-response perspective, cascading two bandpass filters with the same center frequency provides an new bandpass $Q(z^{-1})$, which can have reduced magnitudes at all frequencies outside the passband. This suggests to assign an IIR bandpass $B_0(z^{-1})$ and let $Q(z^{-1}) = Q_0(z^{-1})B_0(z^{-1})$, where $Q_0(z^{-1})$ is the fundamental solution from Section 3.1. Note that (5) indicates the frequency-domain equality

$$1 - e^{-jm\omega}Q_0(e^{-j\omega}) = \frac{A(e^{-j\omega})}{A(\alpha e^{-j\omega})}K(e^{-j\omega}). \tag{12}$$

At $\omega = \omega_0$, we have $A(e^{-j\omega_0}) = 0$ from (8) and hence $Q_0(e^{-j\omega_0}) = e^{jm\omega_0}$ at the center frequency ω_0. Due to this result, $Q_0(z^{-1})$ is not a conventional bandpass filter, and $B_0(z^{-1})$ needs to satisfy $B_0(e^{-j\omega_0}) = 1$ to preserve the property $Q_0(e^{-j\omega_0})B_0(e^{-j\omega_0}) = Q_0(e^{-j\omega_0}) = e^{jm\omega_0}$.

A standard bandpass filter will suffice this requirement. Recall that $A(z^{-1})/A(\alpha z^{-1})$ is a notch filter. One candidate $B_0(z^{-1})$ is $1-\eta A(z^{-1})/A(\alpha z^{-1})$: $\eta \in (0,1]$ (unity minus a notch shape generates a bandpass shape).

Fig. 5 presents the $Q(z^{-1})$ and $1-z^{-m}Q(z^{-1})$ solved from the discussed algorithms in this section. The solid lines are the direct solution from Section 3.1; the dashed lines are from Section 3.2.1; and the dotted lines from Section 3.2.2. We observe from the magnitude responses of $1-z^{-m}Q(z^{-1})$, that all three methods create the required attenuation around 3000 Hz. Also, the additional magnitude constraints on $Q(z^{-1})$ are effectively reflected in the bottom plot of Fig. 5: in the dashed-line $Q(z^{-1})$, the design of $B_0(z^{-1})=1+0.7z^{-1}$ places a zero $z=-0.7$ near the Nyquist frequency ($z=e^{\pi}=-1$), yielding the small gain in the high-frequency region compared to the solid-line $Q(z^{-1})$; in the dotted-line $Q(z^{-1})$, by cascading the bandpass filter $B_0(z^{-1})$ we have reduced the magnitude of $Q(z^{-1})$ at both low and high frequencies.

Finally we note the presence of the "waterbed effect" in Fig. 5, a result of the fundamental limitation of feedback loop shaping. Besides the strong disturbance attenuation around 3000 Hz, the magnitude of $1-z^{-m}Q(z^{-1})$ holds values higher than unity at other frequencies. The fundamental solution (solid line) from Section 3.1 evenly spreads the amplification throughout the entire frequency region; the dashed line has enhanced robustness at high frequencies and makes $1-z^{-m}Q(z^{-1})$ closer to unity near Nyquist frequency; lastly the IIR-$B_0(z^{-1})$ algorithm concentrates the amplification near the center frequency 3000 Hz. In general, it is preferred to evenly spread the amplifications, so the solid or the dashed lines are preferred from the performance perspective. Yet if large model uncertainty exists which enforces $Q(z^{-1})$ to have small magnitudes at high and/or low frequencies, the dotted line may be considered over the other designs. Nonetheless, the maximum amplification among all designs is around 1.6dB (1.2023) while the attenuation is more than -20dB (0.1) in a large frequency region (perfect attenuation at the center frequency 3000 Hz). One way to "smoothen" the waterbed effect is to replace $Q(z^{-1})$ with $kQ(z^{-1})$ at the final stage of design. This will trade off the perfect disturbance attenuation with a less amplified loop shape at other frequencies.

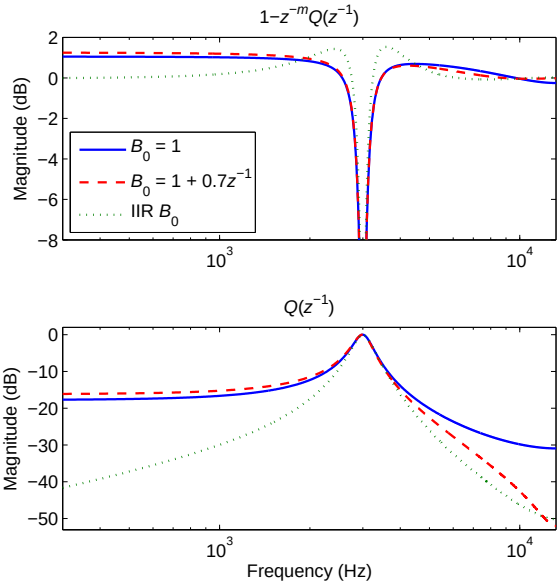

Fig. 5. Comparison of the magnitude responses in three designs of $Q(z^{-1})$ for wide-band disturbances: in the dotted line, $B_0(z^{-1})=1-\alpha A(z^{-1})/A(\alpha z^{-1})$

4. SIMULATION AND EXPERIMENTAL RESULT

4.1 Audio-vibration rejection in HDDs

In this section we apply the discussed control schemes for audio-vibration rejection on a HDD benchmark system (IEEJ, Technical Commitee for Novel Nanoscale Servo Control, 2007). In this case study, the plant dynamics involves a single-stage actuator that is powered by a voice coil motor, and the control aim is to regulate the plant output in the presence of external disturbances. The frequency response of the sampled plant (sampling frequency $F_s=26400$ Hz) is shown in Fig. 6. The multiple resonance modes are attenuated via several notch filters, and the notched plant is treated as $P(z^{-1})$ in Fig. 2. The plant delay in this case is $m=3$. The baseline design $C(z^{-1})$ is a PID controller which achieves a servo bandwidth of 1.19 kHz. The disturbance source is from a scaled version of actual experimental results under audio vibration.

The top plot of Fig. 7 shows the spectrum of the position error signal (PES) without the proposed local loop shaping. To attenuate the main spectral peaks centered at 880 Hz and 1600 Hz, we apply the algorithm in Section 3.1, with a two-band $Q(z^{-1})$, $\alpha=0.945$, and $kQ(z^{-1})=0.8Q(z^{-1})$. Fig. 8 presents the magnitude responses of the loop shaping elements, where we observe the deep attenuation at the desired 880 Hz and 1600 Hz. The bottom plot of Fig. 7 shows the resulted PES, where the spectrum has been greatly flattened compared to the case without compensation, and we can see a direct projection of the shape of $1-z^{-m}Q(z^{-1})$ to the error spectrum. The corresponding time traces are provided in Fig. 9. The three-sigma value (sigma is the standard deviation) has reduced from 33.54% TP (Track Pitch) to 22.79% TP (here 1 TP = 254 nm), i.e., a 29.07 percent improvement. Notice that 1600 Hz is above the bandwidth of the servo system, where disturbance rejection was not feasible for the original feedback design.

Additional customization on $Q(z^{-1})$ is carried out using the discussions in Section 3.2. Table 2 shows the attenuation results on the three-sigma value of the position errors. For all designs in the last three columns, we have enforced $Q(z^{-1})$ to have small gains in the high-frequency region. Actually if the high-frequency gain of $Q(z^{-1})$ is larger than -10 dB the closed-loop becomes unstable. This can be projected by plotting the frequency response of $S(z^{-1})$ and noting that the term $z^{-m}Q(\hat{P}^{-1}P-1)$ is no longer negligible. We observe that all designs provided large servo enhancements by at least 21.85% reduction on the three-sigma values.

Table 2. Comparison of servo enhancement

$B_0(z^{-1})$, i.e., the fixed part in $Q(z^{-1})$	1	$1+z^{-1}$	$1-z^{-2}$	IIR bandpass $1-\alpha A(z^{-1})/A(\alpha z^{-1})$
3σ w/ compensation (%TP)	23.79	24.33	24.76	26.21
3σ reduction (baseline 33.54%TP)	29.07%	27.46%	26.18%	21.85%

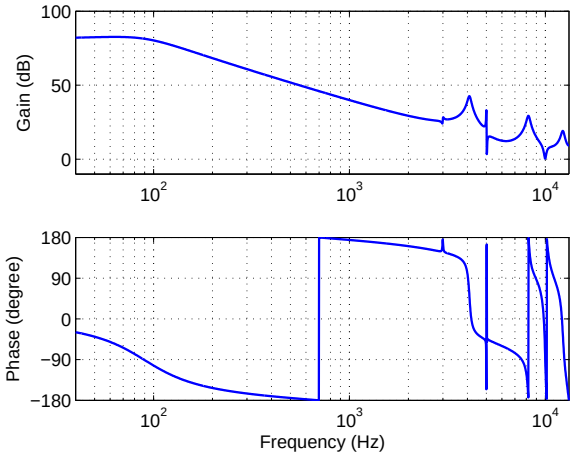

Fig. 6. Frequency response of the plant in the HDD benchmark

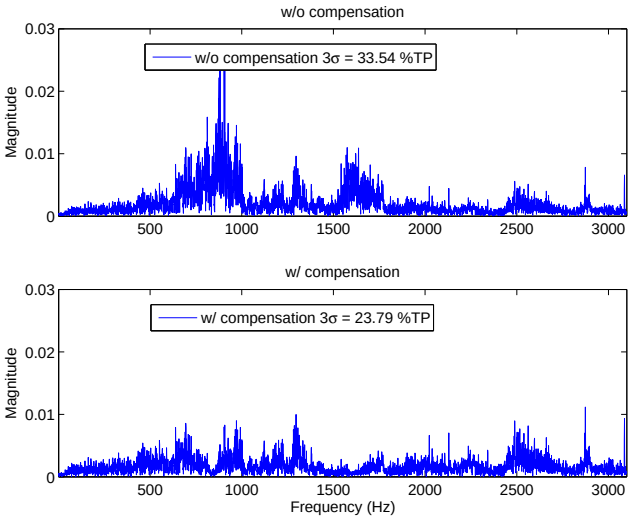

Fig. 7. Spectra (FFT) of the position error signals with and without compensation

4.2 Harmonic cancellation in an EPS system

In this section we apply the algorithm to an electrical-power-steering (EPS) system described in Sugita and Tomizuka (2012). This system features a variable-gear-ratio (VGR) control module for enhanced vehicle steering. VGR control provides speed-dependent assistive torque during steering, to reduce driving effort and to improve driver comfort and safety. The problem of narrow-band disturbance rejection occurs as the VGR system generates unnatural reaction torques and contains imperfections in the gear and motor rotations.

One level of the motion control involves a velocity feedback servo loop, where the motor accepts torque input and the rotational velocity is the output. In this case, the plant under control is $G(s) = 1/(J_m s + B_m)$, where J_m is

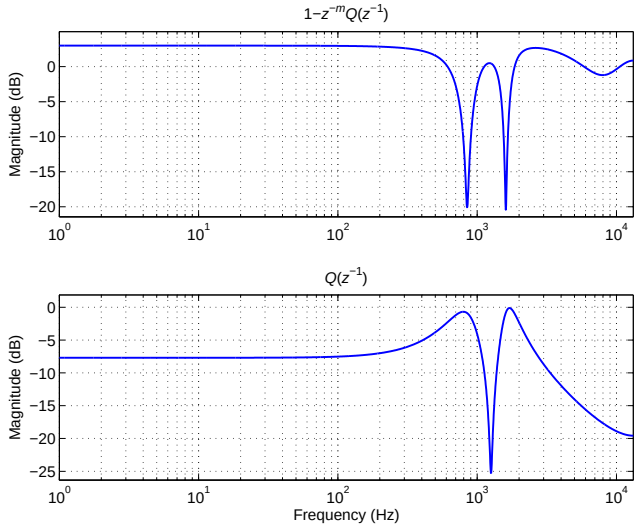

Fig. 8. $1-z^{-m}Q(z^{-1})$ and $Q(z^{-1})$ used for vibration rejection in HDDs

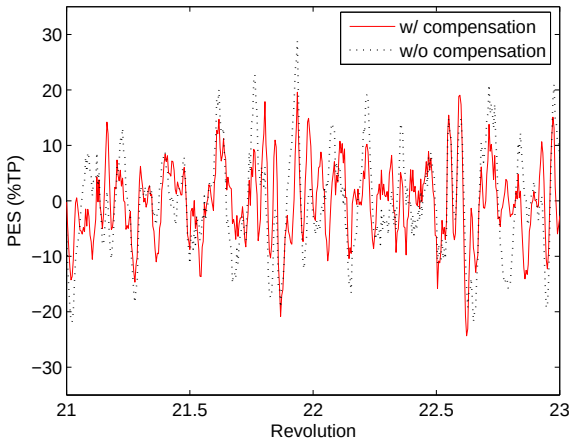

Fig. 9. Time traces of the position error signals with and without compensation

the inertia of the motor and B_m is the friction damping coefficient. This plant is discretized at a sampling time of 1 ms. The system has a 4ms input delay, yielding $m = 4$ in the local loop shaping design.

The top plot of Fig. 10 demonstrates the motor velocity during a variable-speed steering test (experimental results), where we observe large tracking errors between the reference velocity and the actual motor speed. Further investigation shows that there are strong narrow-band vibrations due to imperfect motor rotations. The dashed line in Fig. 11 presents the spectrum of the tracking errors when we apply a constant-speed steering. The strong spectral peak at 15 Hz contributes greatly to the tracking errors. Applying the proposed algorithm in Section 3.1 yields the solid line in Fig. 11. Visual comparison indicates that the

algorithm has removed the original spectral peak at 15 Hz. Computing the standard deviations for the tracking errors, we obtain a 74.77% error reduction on the 3σ value (from 0.20826 rad/s to 0.052549 rad/s). Besides these constant-speed steering results, back to comparing the variable-steering-speed test in Fig. 10, the algorithm also provides significant performance enhancement, both visually and quantitatively (3σ reduces from 0.19402 to 0.102). Here the vibration frequency no longer stays at 15 Hz but actually varies based on the steering speed. An adaptive $Q(z^{-1})$ is used to obtain the bottom plot of Fig. 10, using the identified relationship between the steering speed and the vibration frequency.

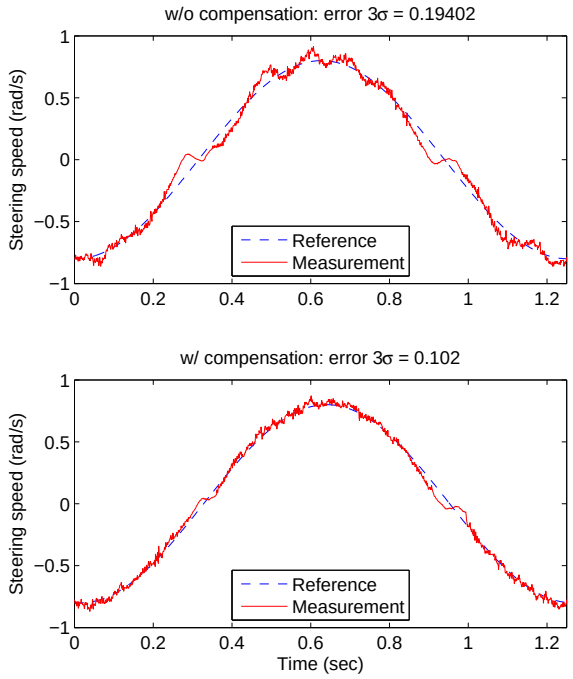

Fig. 10. Time traces of the EPS tracking result during variable-speed steering

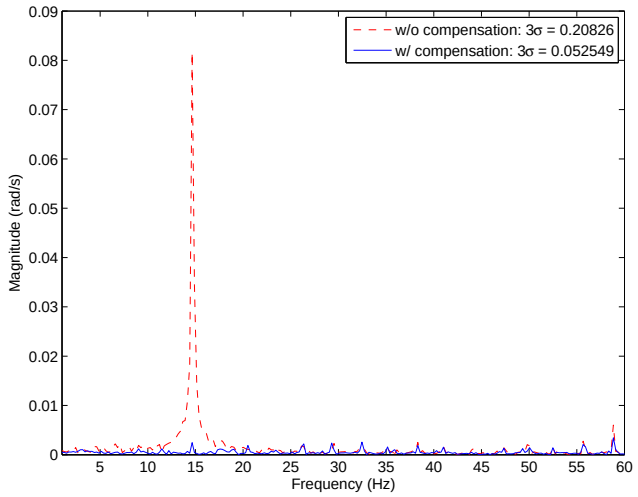

Fig. 11. Spectra of the tracking errors during constant speed steering

5. CONCLUSION

In this paper we have discussed an algorithm for enhancing the servo performance at several bands of frequencies. In the presence of bandwidth limitations in feedback design, such a local loop shaping approach suits well for attenuating strong vibration-type disturbances. Simulation and experimental results support the proposed design and analysis.

6. ACKNOWLEDGMENT

This work was supported in part by the Computer Mechanics Laboratory (CML) in the Department of Mechanical Engineering, University of California at Berkeley.

REFERENCES

Chen, X., Castellanos Silva, A., and Tomizuka, M. (2013). Adaptive model inversion for rejection of time-varying vibrations on a benchmark problem. In *2013 European Control Conference (submitted)*.

Chen, X. and Tomizuka, M. (2012). A minimum parameter adaptive approach for rejecting multiple narrow-band disturbances with application to hard disk drives. *IEEE Transactions on Control System Technology*, 20(2), 408 –415. doi:10.1109/TCST.2011.2178025.

Chew, K. and Tomizuka, M. (1989). Digital control of repetitive errors in disk drive systems. In *Proceedings of the 1989 American Control Conference*, 540–548. IEEE.

Cuiyan, L., Dongchun, Z., and Xianyi, Z. (2004). A survey of repetitive control. In *Proceedings of 2004 IEEE/RSJ International Conference on Intelligent Robots and Systems.*, volume 2, 1160–1166. IEEE.

Deller, J.R., Hansen, J.H.L., and Proakis, J.G. (1999). *Discrete-time processing of speech signals*. Wiley-IEEE Press.

Ehrlich, R. and Curran, D. (1999). Major HDD TMR sources and projected scaling with TPI. *IEEE Transactions on Magnetics*, 35(2), 885–891.

Guo, L. and Chen, Y.J. (2001). Disk flutter and its impact on hdd servo performance. *IEEE Transactions on Magnetics*, 37(2), 866 –870. doi:10.1109/20.917633.

IEEJ, Technical Commitee for Novel Nanoscale Servo Control (2007). NSS benchmark problem of hard disk drive systems. http://mizugaki.iis.u-tokyo.ac.jp/nss/.

Landau, I.D., Constantinescu, A., and Alma, M. (2009). Adaptive regulation-Rejection of unknown multiple narrow band disturbances. In *17th Mediterranean Conference on Control & Automation*, 1056–1065. IEEE.

Landau, I.D. and Zito, G. (2006). *Digital control systems: design, identification and implementation*. Springer Verlag.

Ohnishi, K., Shibata, M., and Murakami, T. (1996). Motion control for advanced mechatronics. *IEEE/ASME Trans. Mechatronics*, 1(1), 56 –67. doi:10.1109/3516.491410.

Shoureshi, R. and Knurek, T. (1996). Automotive applications of a hybrid active noise and vibration control. *IEEE Control Systems Magazine*, 16(6), 72–78.

Skogestad, S. and Postlethwaite, I. (2005). Multivariable feedback control analysis and design. *New York*.

Sugita, S. and Tomizuka, M. (2012). Cancellation of unnatural reaction torque in variable-gear-ratio. *Journal of*

Dynamic Systems, Measurement, and Control, 134(2), 021019.

Tomizuka, M. (1987). Zero phase error tracking algorithm for digital control. *ASME Journal of Dynamic Systems, Measurements, and Control*, 109(1), 65–68.

Tomizuka, M. (2008). Dealing with periodic disturbances in controls of mechanical systems. *Annual Reviews in Control*, 32(2), 193 – 199. doi: 10.1016/j.arcontrol.2008.07.002.

Zheng, J., Guo, G., Wang, Y., and Wong, W. (2006). Optimal narrow-band disturbance filter for pzt-actuated head positioning control on a spinstand. *IEEE Transactions on Magnetics*, 42(11), 3745–3751.

Zhou, K. and Doyle, J.C. (1998). *Essentials of robust control*. Prentice Hall New Jersey.